Designing double isolated bands and subgap states in two-dimensional $X\mathrm{PS_3}$ (X = Al, Ga, In, Tl) for achieving bi-anti-ambipolar transport

Jialin Yang,[1] Chuyao Chen,[1] Xuemin Hu,[1,2,*] Tingting Guo,[1] Hengze Qu,[1,†] Zhenhua Wu,[3] Li Tao,[4] and Shengli Zhang[1,‡]

[1] *MIIT Key Laboratory of Advanced Display Materials and Devices, College of Material Science and Engineering, Nanjing University of Science and Technology, Nanjing 210094, P. R. China*

[2] *School of Material Engineering, Jinling Institute of Technology, Nanjing 211169, China*

[3] *Key Laboratory of Microelectronics Device and Integrated Technology, Institute of Microelectronics of Chinese Academy of Sciences, Beijing 100029, China*

[4] *School of Materials Science and Engineering, Jiangsu Key Laboratory of Advanced Metallic Materials, Center for 2D Materials, and Center for Flexible RF Technology, Southeast University, Nanjing 211189, China*

(Received 28 February 2024; revised 21 April 2024; accepted 10 May 2024; published 5 June 2024)

Anti-ambipolar transistors (AATs) are a promising candidate for multivalued logic devices, which are vital for improving the device density and data-handling capabilities of nanoelectronics. Compared with most AATs with Λ-shaped transport characteristics, the emerging four-logic-state bi-AATs have a stronger capability for exponentially increasing the integration density. Here, we demonstrate an alternative strategy to achieve bi-anti-ambipolar transport by using the intrinsic electronic properties of two-dimensional (2D) materials. In detail, by breaking symmetry in edge-sharing octahedra, 2D $X\mathrm{PS_3}$ (X = Al, Ga, In, Tl) materials exhibit isolated band structures with subgap states near the Fermi level. More importantly, this special electronic feature inspires the design of double subgap tunnel field-effect transistors (TFETs) for realizing bi-anti-ambipolar transport. Through quantum transport simulations, we observe M-shaped *I-V* curves in the 2D $\mathrm{InPS_3}$ TFET, verifying the feasibility of the device concept. This work broadens the horizon for the development of bi-anti-ambipolar devices in the forthcoming era of big data.

DOI: 10.1103/PhysRevApplied.21.064009

I. INTRODUCTION

According to Moore's Law and von Neumann architecture, the continuous expansion of device density has gradually reached a bottleneck, posing higher demands for data processing [1,2]. To address this issue, the multivalued logic (MVL) circuit is proposed as an effective approach to reduce the burden of high-density integration without the further scaling of transistors [3]. In particular, the anti-ambipolar transistor (AAT) has been recognized as a promising candidate for constructing MVL devices due to its special nonmonotonic transfer characteristics and negative differential resistance (NDR) effects enabling multivalued operation [4–10]. Compared with conventional binary logic circuits, AATs possess more than three logic states, and so have higher capabilities for data processing and large-scale integration [11,12]. The development of AATs brings hope for the forthcoming era of big data.

Artificially stacking different two-dimensional (2D) materials to form *p-n* heterojunctions is one of the emerging mainstream approaches for achieving anti-ambipolar transport [13–17]. Among them, devices with double-peaked M-shaped curves have more potential for building quaternary inverters to further improve integration levels compared with the normal three-logic-state devices [18–21]. For instance, through structural engineering and parallel device configuration, Lim *et al*. have successfully built a $\mathrm{WS_2}$-graphene-$\mathrm{WSe_2}$ heterostructure to achieve double-peak NDR operation [18]. Paul Inbaraj *et al*. have achieved bi-anti-ambipolar switching in a $\mathrm{InSe/WSe_2}$ heterojunction with two transport contributions controlled by proper mechanical strain [19]. For ongoing research, the feasibility of M-shaped characteristics depends on the development of new concepts for devices, suitable combinations of *n*- and *p*-channel materials, and proper regulation strategies [12,22]. Therefore, realizing four-logic-state devices can be complex. Moreover, the precise carrier transport mechanism underlying AATs remains unclear [22], and there are still few MVL devices with more than three logic states, leaving room for discovery. Thus, aiming at exploring novel four-logic-state MVL devices

*Corresponding author: huxm@jit.edu.cn
†Corresponding author: quhz@njust.edu.cn
‡Corresponding author: zhangslvip@njust.edu.cn

with more feasibility and simpler implementation conditions, we wonder whether there is a type of material that can achieve bi-anti-ambipolar transport solely based on its intrinsic properties.

Herein, following the track based on material design and new device concepts, we propose to adopt double subgap materials for achieving bi-anti-ambipolar transport. Through first-principles calculations, we first design a new group of 2D $X\mathrm{PS_3}$ ($X = \mathrm{Al}$, Ga, In, Tl) materials based on the typical structure of metal phosphorus trichalcogenides. The double isolated bands with subgap states near the Fermi level are realized in 2D $\mathrm{GaPS_3}$ and $\mathrm{InPS_3}$. Then, we discuss that the isolated band formation depends on symmetry breaking in edge-sharing octahedra and different orbital interactions in 2D $X\mathrm{PS_3}$. Next, we demonstrate the new device concept to achieve bi-anti-ambipolar characteristics by introducing double subgap states in traditional tunnel field-effect transistors (TFETs). Finally, based on quantum transport simulations, we successfully achieve the M-shaped transfer characteristics in the 2D $\mathrm{InPS_3}$ TFET, and reveal the transport mechanism of bi-anti-ambipolar switching. These findings represent a step toward the development of computing MVL technology beyond three logic states.

II. COMPUTATIONAL METHODS

The geometric optimization and electronic properties of 2D $X\mathrm{PS_3}$ are calculated using density-functional theory (DFT) implemented in the ATOMISTIX TOOLKIT package [23]. The generalized gradient approximation in the Perdew-Burke-Ernzerhof (PBE) functional is used to describe the exchange-correlation interaction [24]. The norm-conserving PseudoDojo pseudopotentials are adopted as the basis set with the density mesh cutoff of 75 hartree. For structural optimization, the tolerance is limited to less than 0.1 GPa for the stress error and 0.02 eV/Å for the force tolerance. The dense $9 \times 9 \times 1$ k-point sampling is adopted for calculation. The vacuum layer of 40 Å is employed to prevent interactions between periodic boundaries.

The transport properties are simulated through DFT coupled with the nonequilibrium Green's function (NEGF) method. The Brillouin zone in the x, y, and z directions is sampled with $30 \times 1 \times 120$ meshes for the device. In the transport simulation process, the periodic, Neumann, and Dirichlet boundary conditions are adopted for the transverse, vertical, and transport directions, respectively. The temperature is set to 300 K. The double-zeta plus polarization (DZP) basis is adopted for the transport calculation to save computational costs. It should be noted that the DZP basis set is comparable to PesudoDojo in the accuracy of electronic properties, which can be seen in Fig. S1 in the Supplemental Material [25]. The computed drain current under a given gate voltage (V_G) and bias voltage (V_{DS}) is calculated based on the Landauer-Büttiker equation [26] as follows:

$$I_{DS}(V_{DS}, V_{GS}) = \frac{2e}{h}\int_{-\infty}^{+\infty}\{T(E, V_{DS}, V_{GS}) [f_S(E - E_{FS}) - f_D(E - E_{FD})]\}dE, \quad (1)$$

where T (E, V_{DS}, V_{GS}) stands for the transmission coefficient, f_S and f_D are the Fermi-Dirac distribution functions of source and drain, and E_{FS} and E_{FD} refer to the electrochemical potential of source and drain electrode, respectively. The difference between E_{FS} and E_{FD} is equal to $e \times V_{DS}$. $T(E)$ refers to the transmission coefficient, which is the average of k-dependent transmission coefficients, and can be obtained from

$$T_{k_{ll}}(E) = \mathrm{Tr}[G^S_{k_{ll}}(E)G_{k_{ll}}(E)G^D_{k_{ll}}(E)G^\dagger_{k_{ll}}(E)], \quad (2)$$

where $G^{S,D}_{k_{ll}}(E) = i(\Sigma_{S,D} - \Sigma^\dagger_{S,D})$ represents the broadening width deriving from source or drain in the form of self-energy $\Sigma_{S,D}$. $G_{k_{ll}}(E)$ and $G^\dagger_{k_{ll}}(E)$ are the retarded and advanced Green's function, respectively. It is must be noted that the optimum ballistic condition at the ultrascaled channel length is assumed in our work. The behaviors of the devices would be degraded after considering various scattering mechanisms. Therefore, our work can be regarded as the upper limit within the assumed ballistic tunneling transport.

III. RESULTS AND DISCUSSION

The atomic structure of 2D $X\mathrm{PS_3}$ is shown in Fig. 1(a). In the side view, there are two sublayers of S atoms, one located at each side, and octahedrally coordinated X atoms and pairs of P atoms located between the S atoms. From the top view, the graphene-like honeycomb arrangement of the X atoms is distributed around the $(\mathrm{P_2S_6})^{4-}$ bipyramids. For X atoms, they can be divided into X_A and X_B subgroups according to the different octahedral patterns. Given this framework, the characteristics of the $X\mathrm{PS_3}$ structures lie in the values of lattice constant, the P-P distance, P-S distance, and X-S distance (X_A-S and X_B-S). The specific values are summarized in Fig. S2 within the Supplemental Material [25]. Naturally, the lattice constants and bond lengths increase to accommodate with the increasing radius of X atoms, except for the P—S bonds, which are slightly compressed.

Compared with the typical $M\mathrm{PS_3}$ ($M = \mathrm{Mg}$, Cr, Mn, Fe, Co, Ni, Cu, Zn, and Cd) structure [27–31], $X\mathrm{PS_3}$ is characterized by the different $(\mathrm{P_2S_6})^{4-}$ bipyramid. As shown in Fig. 1(b), the top and bottom S trimers exhibit a relative in-plane twist of 60° in the $M\mathrm{PS_3}$ lattice, while in $X\mathrm{PS_3}$, the S trimers twist to a greater extent by 20° on the original basis. This process also brings a significant geometric change of the edge-sharing octahedra.

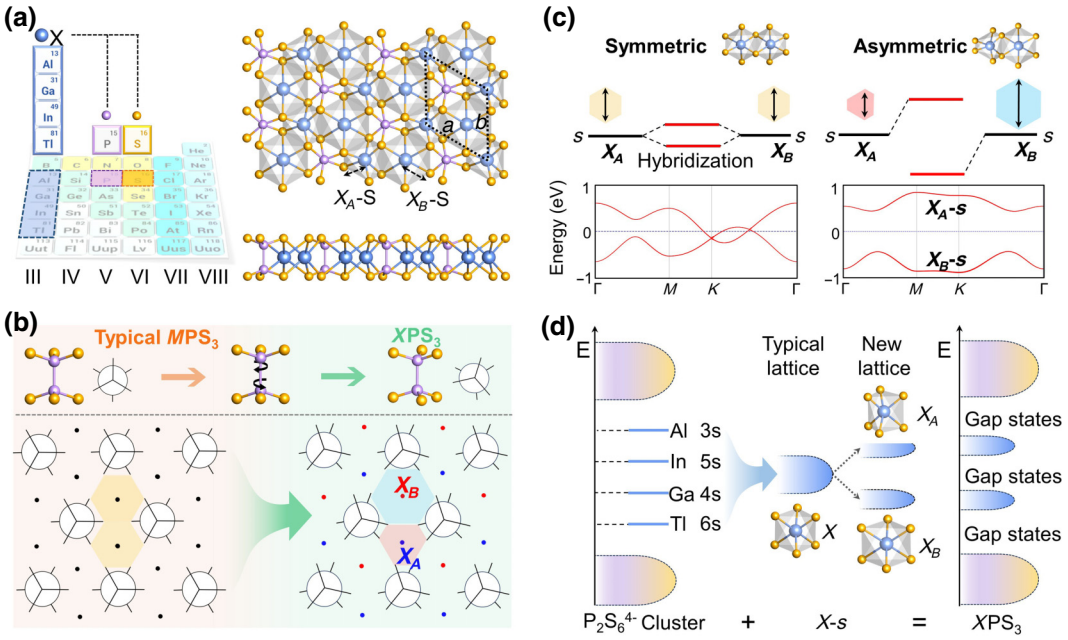

FIG. 1. (a) Top and side views of the geometric structure of monolayer $X\mathrm{PS_3}$ (X = Al, Ga, In, Tl). The dashed rhombus represents the primitive cell. (b) Schematic diagram of the $(\mathrm{P_2S_6})^{4-}$ unit and array transformation from typical $M\mathrm{PS_3}$ to $X\mathrm{PS_3}$. The model represented by the circle and sticks refers to the $(\mathrm{P_2S_6})^{4-}$ bipyramid. The black points represent the metal atoms. The red and blue points represent two types of X atoms in different octahedra, respectively. (c) The state evolution of symmetric and asymmetric edge-sharing octahedra in $M\mathrm{PS_3}$ and $X\mathrm{PS_3}$ lattices. (d) Schematic diagram for realizing isolated bands. The purple and yellow colors refer to the density of states (DOS) contributed by $(\mathrm{P_2S_6})^{4-}$, and the blue color refers to the DOS contributed by X-s orbitals.

In the array diagram shown in Fig. 1(b), M atoms are located in periodic regular octahedra, and the edge-sharing octahedra (yellow hexagonal pattern) maintain high symmetry. However, for the $X\mathrm{PS_3}$ array, one octahedron (blue hexagonal pattern) is expanded, while the other (red hexagonal pattern) is contracted and has a relative in-plane twist, leading to the asymmetry of edge-sharing octahedral structure.

Such symmetry breaking and deformations in edge-sharing octahedra are recognized to have a significant impact on orbital properties [32,33], which is crucial for achieving isolated bands in our work. As plotted in Fig. 1(c), in a typical $M\mathrm{PS_3}$ lattice (with symmetric edge-sharing octahedra), the X_A-s state hybridizes with the X_B-s state near the Fermi level. However, in the optimized $X\mathrm{PS_3}$ lattice, the asymmetric octahedral ligand field leads to the split of X-s states, resulting in difficulty in hybridization between the lower X_B-s state and much higher X_A-s state. Figure S3 within the Supplemental Material [25] shows the projected band structures of Al-, Ga-, In-, and Tl-s orbitals in the two types of lattices. In this case, since the energy levels of the X-s orbitals localize in the gap states of $(\mathrm{P_2S_6})^{4-}$ [34,35], it is expected that the asymmetric edge-sharing octahedra will induce isolated bands near the Fermi level dominated by X_A-s and X_B-s orbitals, as displayed in Fig. 1(d).

Therefore, having identified the role of the geometric structure of the $X\mathrm{PS_3}$ monolayer for realizing isolated bands, we then investigate their electronic properties. As shown in Fig. 2, the band-edge dispersions for the four materials exhibit shapes similar to an isotropic volcano. The 2D $X\mathrm{PS_3}$ materials are semiconducting with quasidirect band gaps (E_g) of 0.56–0.84 eV at the PBE level, with the conduction band minimum (CBM) and the valence band maximum (VBM) both lying at the "volcanic vent" (Γ-M and Γ-K paths). The intrinsic isolated bands near the Fermi level are observed in $X\mathrm{PS_3}$ as expected. In detail, $\mathrm{AlPS_3}$ and $\mathrm{TlPS_3}$ with small E_g show only the isolated highest valance band (IVB) and isolated lowest conduction band (ICB), respectively. Meanwhile, a remarkably large subgap below the IVB (E_{SGV}) of 1.8 eV and subgap above the ICB (E_{SGC}) of 1.69 eV can be observed in $\mathrm{AlPS_3}$ and $\mathrm{TlPS_3}$, respectively. In contrast with the one-sided situation, 2D $\mathrm{GaPS_3}$ and $\mathrm{InPS_3}$, which have larger E_g, show isolated states for both the lowest conduction bands (LCBs) and the highest valance bands (HVBs), along with double subgap states. In particular, for 2D $\mathrm{InPS_3}$, the volcanic dispersions of the ICB and IVB are extremely similar, and the widths of the ICB (W_{IC}) and IVB (W_{IV}) differ by only 0.03 eV (see more detail on parameters in Table S1 within the Supplemental Material [25]). Moreover, taking the impact of spin-orbit coupling into account, there

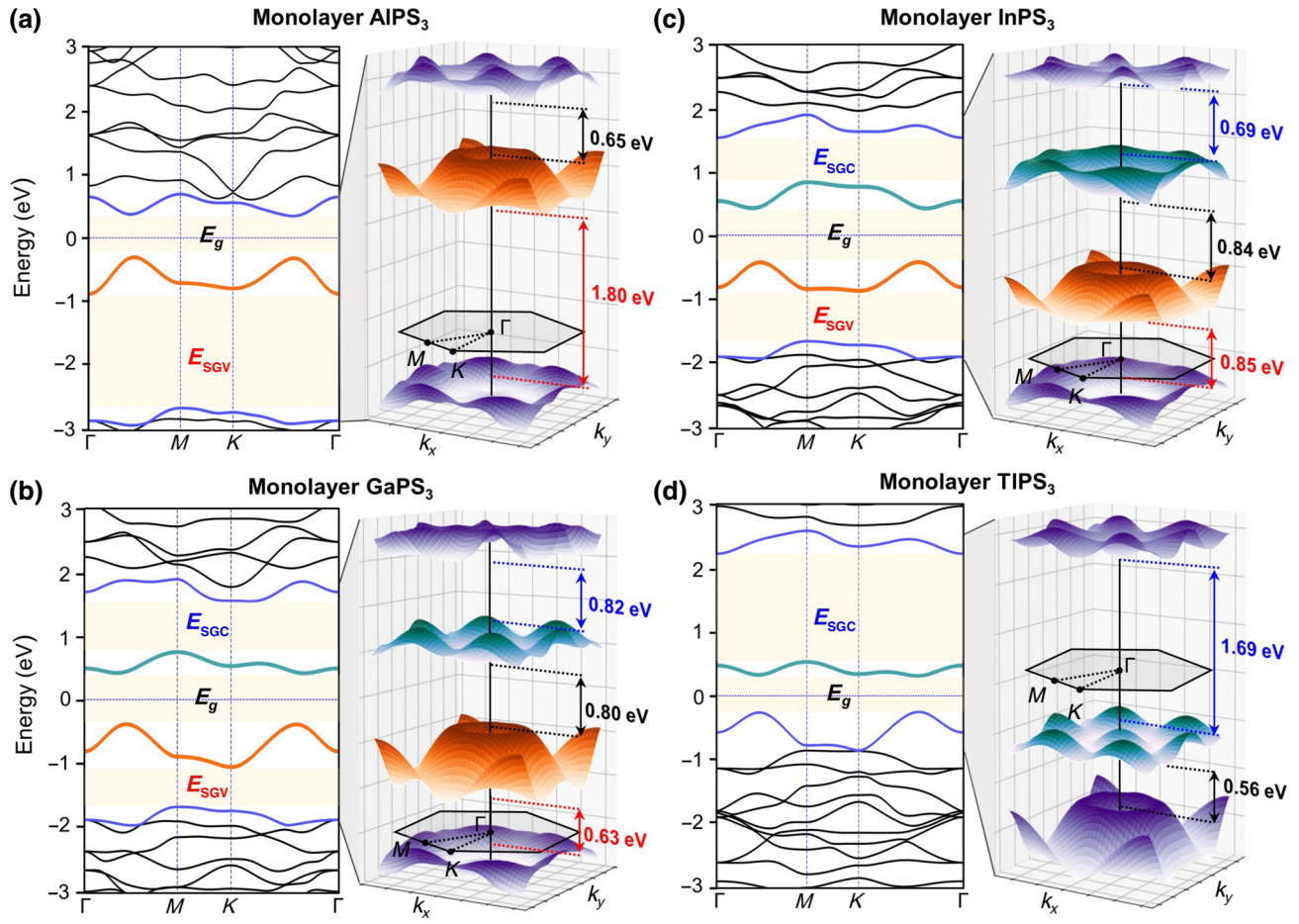

FIG. 2. Band structures (left) and three-dimensional dispersions (right) of 2D (a) $AlPS_3$, (b) $GaPS_3$, (c) $InPS_3$, and (d) $TlPS_3$. The dispersions in green and orange represent the isolated lowest conduction bands (ICB) and highest valance bands (IVB), respectively. The dispersions in purple refer to neighbor nonisolated states. Yellow regions refer to the gap states of band gaps (E_g), subgap above the ICB (E_{SGC}), and subgap below the IVB (E_{SGV}).

is no obvious band splitting or dispersion change affecting the isolated bands near the Fermi level (see Supplemental Material, Fig. S4 [25]).

To throw light on the origin and differences of the isolated bands and subgap states in $X\mathrm{PS}_3$, we further calculate the projected density of states (PDOS) and partial charge densities. In Fig. 3(a), depending on the specific composition and geometric location in the unit cell, S-p orbitals contribute to all states and dominate the deep energy level. X-s orbitals significantly contribute to the band-edge states and hybridize with S-p orbitals. The partial charge densities of the LCB, HVB, and their neighbor states are calculated to determine the specific atomic contribution. As displayed in Fig. 3(b), the $(P_2S_6)^{4-}$ unit accounts for a large proportion in the charge states, but it seems that only the S atoms in $(P_2S_6)^{4-}$ mainly contribute to the states below the Fermi level. Remarkably, the spherical X_A-s and X_B-s states contribute to the LCB and HVB, respectively, which is consistent with the analysis in Fig. 1. The specific charge densities of each $X\mathrm{PS}_3$ are shown in Fig. S5 within the Supplemental Material [25].

The similar charge densities are insufficient to explain the disappearance of isolated states in $AlPS_3$ and $TlPS_3$. Thus, from the perspective of orbital energy, we further calculate the energy-level aligned PDOS. Without considering the hybridization with X-s orbitals, the intrinsic energy edges of $(P_2S_6)^{4-}$ are shown as the black dashed lines in Fig. S5 within the Supplemental Material [25], which exhibits no significant difference in energy levels among the four $X\mathrm{PS}_3$. X-p orbitals with spindle orbitals heavily overlap with S-p orbitals, and end up with their energy distribution localized as $(P_2S_6)^{4-}$, which can be observed in the right panels of Fig. 3(c). Unlike the X-p orbitals, the spherical X-s orbitals are less affected by the $(P_2S_6)^{4-}$ unit. Despite the strong hybridization with S-p orbitals, the energy distribution of X-s orbitals mainly depends on the intrinsic orbital energy. Therefore, as shown in Fig. 3(c), from Al to Tl, X-s orbitals (green panels) tend to move towards lower energy levels, while

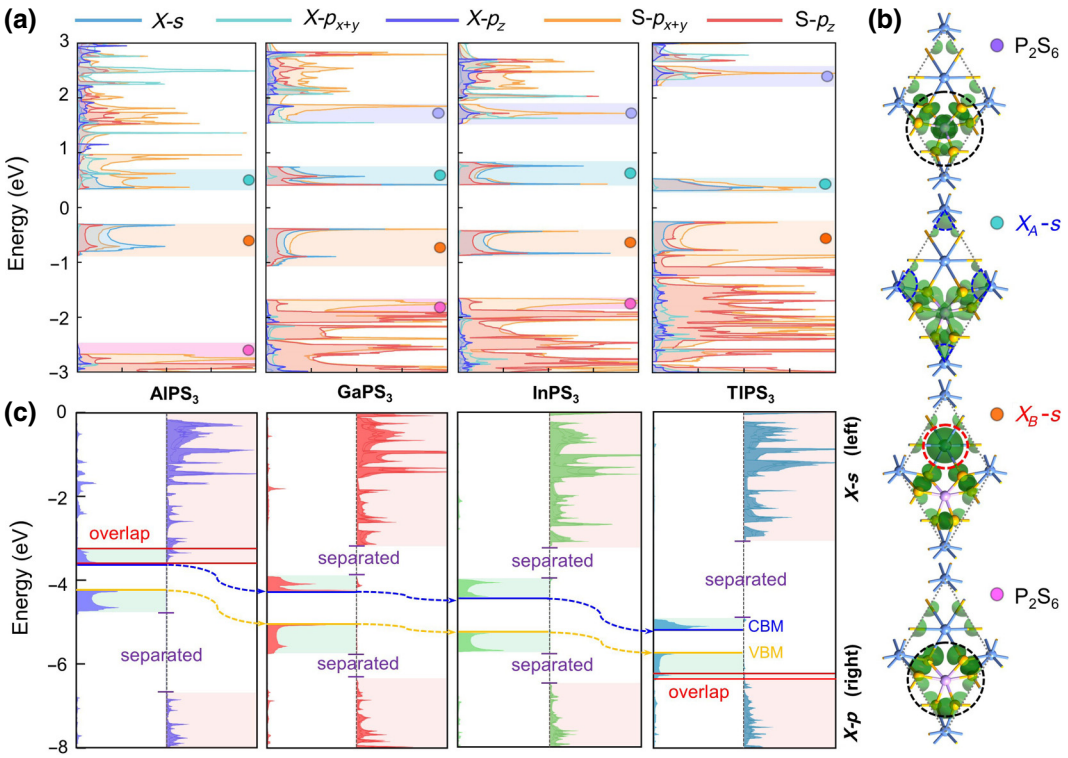

FIG. 3. (a) Orbitally projected density of states (PDOS) of 2D $X\mathrm{PS}_3$. (b) The partial charge densities are displayed along with their respective energy levels, which are labeled on the PDOS diagram. (c) Energy level aligned X-s (left panel) and X-p (right panel) orbital-resolved PDOS. Blue and yellow lines represent conduction band minimum (CBM) and the valence band maximum (VBM), respectively. The energy level positions have been corrected by vacuum level.

the energy of X-p orbitals is almost fixed during this process. In this case, the Al_A-s with the highest energy and the Tl_B-s with the lowest energy overlap with other orbitals, resulting in continuity of energy and disappearance of gap states. Ga-s and In-s, with energy in the middle, possess both ICB and IVB. The summarized band alignment of the four $X\mathrm{PS}_3$ are also shown in Fig. S6 within Supplemental Material [25].

Based on the novel electronic properties, we propose to use the isolated bands near the Fermi level and double subgap states to achieve the rare bi-anti-ambipolar characteristic. The concept and ON-OFF mechanism of the double subgap TFETs are depicted in Fig. 4. On the basis of the classical ambipolar TFET [36], we introduce double subgap states in the source, channel, and drain regions. The bias voltage (supply voltage V_{DS}) is added to obtain the energy overlap between the valance band in the p-doped source and the conduction band in the n-doped drain for achieving band-to-band tunneling, as shown in the narrow green region in Fig. 4. In the initial state (V_{G1}), the band gap in the channel blocks the tunneling path. Then, by applying a positive gate voltage (V_{G2}), the conduction band of the channel is dragged down below the VBM in the source, and the conductive tunneling path is wide open to realize an n-type ON state. So far, this is just a regular switching process of the n-type TFET. However, continuously increasing the positive gate voltage (V_{G3}), the tunneling path starts to shrink as soon as the E_{SGC} in the channel has been pulled down into the green region. With the larger positive gate voltage (V_{G4}), the current continues to decrease until the gap states in the E_{SGC} completely block the tunneling path, then the device shuts down once again, achieving the anti-ambipolar switching. The whole process is shown in Figs. 4(a)–4(d). Moreover, in Fig. 4(e), taking the E_{SGV} in the channel into account, applying more negative gate voltages can also realize the anti-ambipolar transport for holes. In this way, the bi-anti-ambipolar transport can be achieved with intrinsic double subgap states in channel materials.

To obtain better bi-anti-ambipolar characteristics, it is necessary to comprehensively consider the electronic properties of specific materials and operating voltages of the device. In detail, as illustrated in Fig. 4(a), we define the energy overlap between the ICB and IVB as the tunneling path width (W_{T}), which can be written as

$$W_{\mathrm{T}} = W_{\mathrm{IC}} + W_{\mathrm{IV}} + \Delta E_1 + \Delta E_2 - V_{DS}, \tag{3}$$

where ΔE_1 and ΔE_2 are the energy difference between the VBM and Fermi level in the source (E_{FS}), and between the

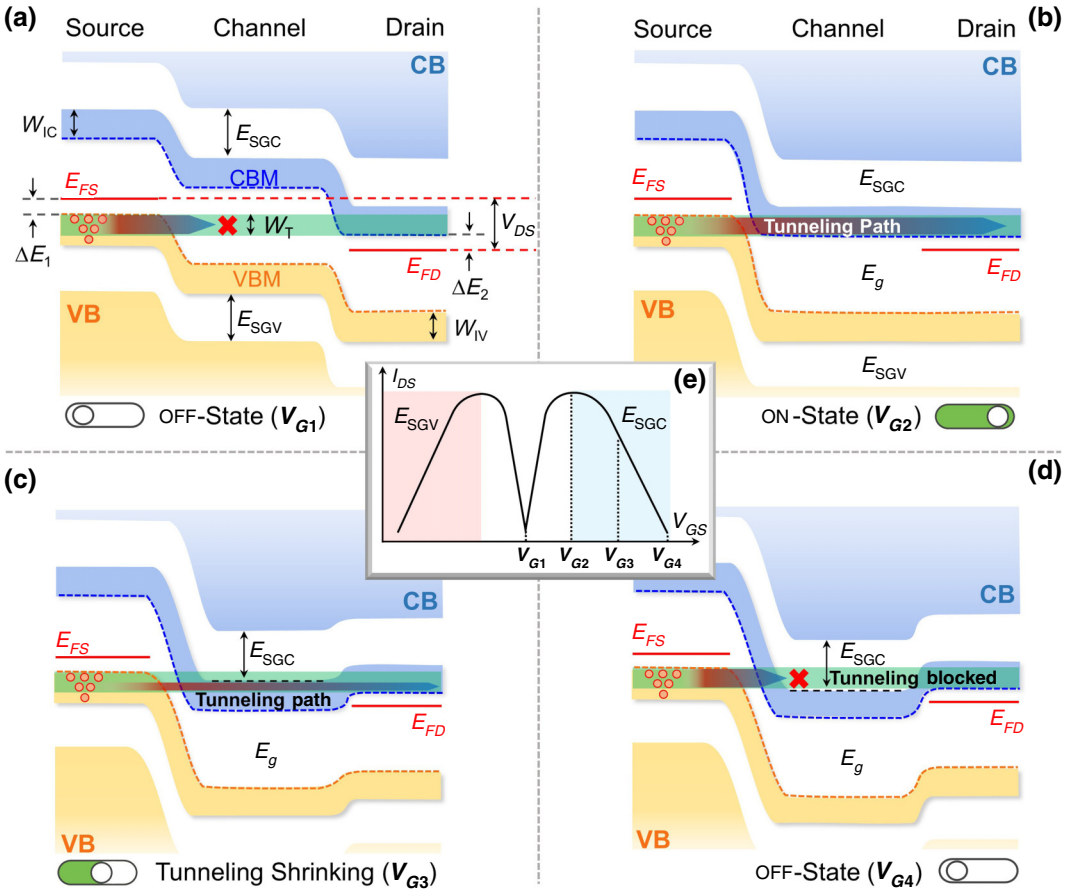

FIG. 4. (a)–(d) Schematic energy-band diagrams of the double subgap TFET under increasing positive gate voltage from V_{G1} to V_{G4}. E_{FS} and E_{FD} are the Fermi level of source and drain. Blue and orange dashed lines represent CBM and VBM, respectively. (e) The schematic diagram of M-shaped transfer I-V characteristic. The red and blue panels refer to regions where E_{SGV} and E_{SGC} work, respectively.

CBM and Fermi level in drain (E_{FD}), respectively, which are determined by the doping level. For a certain isolated-band material, W_T can be adjusted by the doping level and the V_{DS}, and the setting of W_T depends on the gate control capability and the device performance requirements. Specifically, a wide W_T can lead to more tunneling states and higher ON-current, but a large V_{GS} is required to drag the deep gap states to block the tunneling, also leading to large driving range (ΔV). In contrast, a small W_T will induce a lower ON-current, while it is easier for the gap states to cut off the tunneling path and turn off the device. Moreover, the W_T should be set smaller than E_{SGC} and E_{SGV} to avoid current leakage, because the subgap states are insufficient to block the entire tunneling window if the W_T is too large.

In the preceding discussion, we qualitatively illustrate the operation mechanism of bi-anti-ambipolar transport in the double subgap TFET on the basis of a schematic energy-band diagram. According to this theory, the bi-anti-ambipolar characteristic is equally affected by the ICB and IVB, and the wide isolated bands ($W_{IC} + W_{IV}$) are not preferred because of their stronger demand for V_{DS} to get the required W_T. To present an ideal transport characteristic, we choose to adopt 2D $InPS_3$ as the channel material for further atomic-scale transport calculations, owing to its symmetric and narrow isolated bands. Moreover, we compute the phonon spectrum of 2D $InPS_3$, as shown in Fig. S7 within the Supplemental Material [25], and find no imaginary phonon modes, which indicates that it is dynamically stable. The device model can be found in Fig. S8 within the Supplemental Material [25]. The 2D $InPS_3$ is sandwiched between the top and bottom dielectric layers ($\varepsilon = 3.9$) and metal gates. The symmetric doping concentration of 5×10^{13} cm^{-2} is used in the p-doped source and n-doped drain. The channel length is set to 7 nm. Additionally, an underlap region of 4 nm, which is the spacer between the gate and source (drain), is adopted as the buffer area for band bending.

First, calculated I_{DS}-V_{DS} curves are presented in Fig. 5(a) for studying the output characteristics. N-shaped

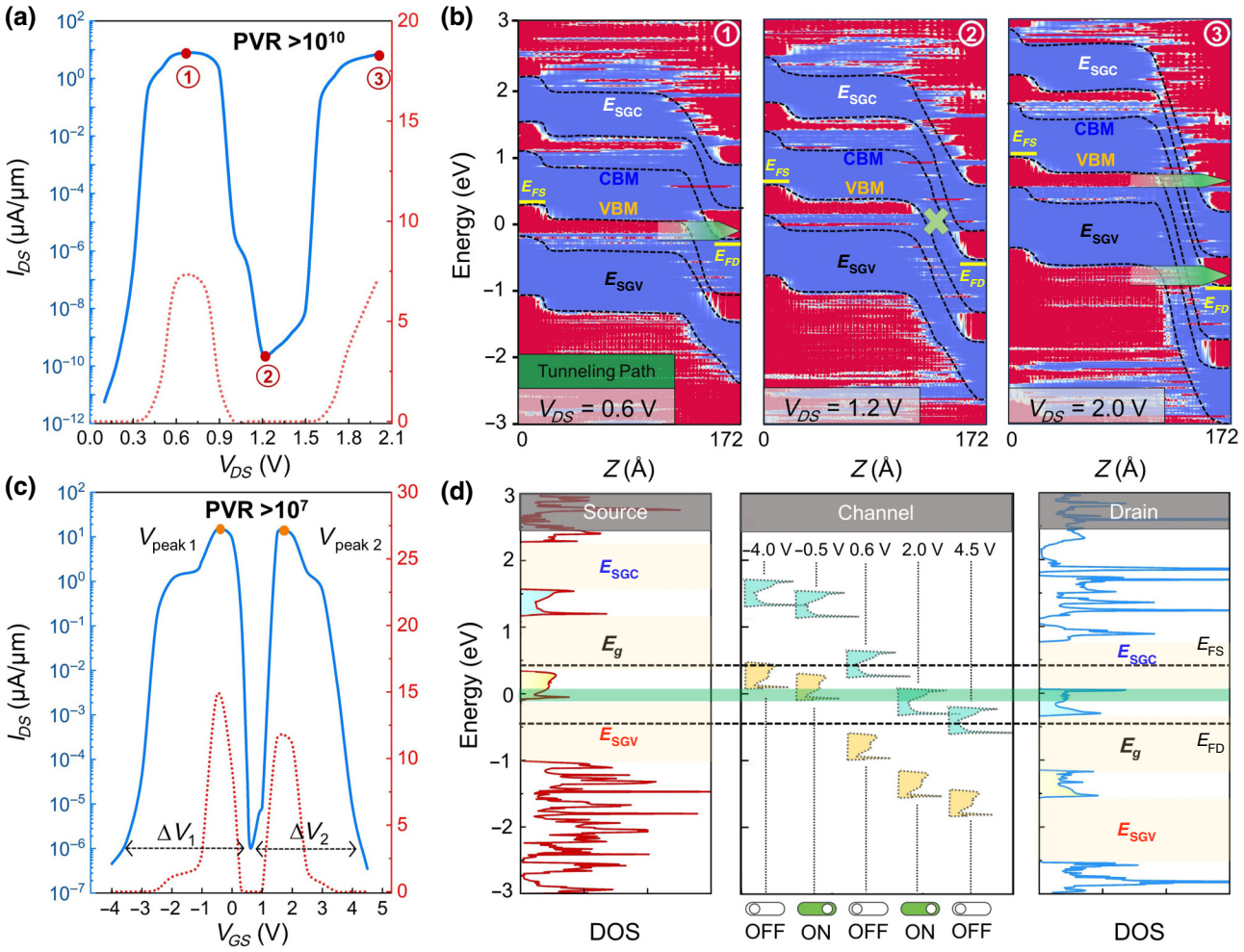

FIG. 5. (a) I_{DS}-V_{DS} characteristics of the 2D $InPS_3$ double subgap TFET. (b) Position-resolved local density of states (LDOS) for ON, OFF, ON states at V_{DS} of 0.6, 1.2, 2.0 V, respectively. E_{FS} and E_{FD} represent the Fermi level of the left source and right drain. The green arrows represent the tunneling path. (c) I_{DS}-V_{GS} characteristics of the 2D $InPS_3$ double subgap TFET. (d) The device density of states (DDOS) of source and drain in left and right panels. The middle panel represents the channel DDOS aligned with source and drain under different V_{GS}. The blue and yellow DDOS regions refer to the contributions of ICB and IVB, respectively. The green region represents the energy overlap region inside the bias window between the ICB in the source and the IVB in the drain.

curves and a remarkable NDR effect can be observed with a high peak-to-valley current ratio (PVR) of over 10^{11}. The underlying mechanism is shown as the position-resolved local density of states (LDOS) in Fig. 5(b). According to the Fermi-Dirac distribution, the carrier occupation probability remains at 1 inside the bias window (E_{FS}–E_{FD}, equal to V_{DS}), and gradually degenerates far away from the bias window [37]. Once an available tunneling path is opened in the bias window, the current can be boosted. As V_{DS} changes from 0.6 to1.2 V, the increasing V_{DS} pulls the IVB in the source and the ICB in the drain apart, and this results in the E_{SGC} in the drain blocking the tunneling path. From 1.2 to 2.0 V, the V_{DS} pushes the E_{SGC} in the drain below the IVB in the source, and the ICB in the drain below the E_{SGV} in the source and channel. Thus, the energy states can link the source to the drain, creating two new tunneling paths in a large bias window.

Second, to study the bi-anti-ambipolar transport, we set the V_{DS} to 0.85 V and limit the W_T to 0.15 eV for achieving a smaller ΔV and higher PVR. As shown in Fig. S9 within the Supplemental Material [25], at the same V_{GS}, the high V_{DS} easily suppresses the drain current (I_{DS}) to a low level, as we mentioned in the former discussion. The transfer characteristics are shown in Fig. 5(c). The M-shaped curves indicate the successful realization of the bi-anti-ambipolar characteristic. The left and right driving ranges (ΔV_1 and ΔV_2) are only 4.2 and 3.7 V, and the operation voltages (V_{peak1} of −0.4 V and V_{peak2} of 1.6 V) lie at the small voltage range close to the initial state. The PVR reaches over 10^7. Moreover, the calculated subthreshold swing for I_{DS}-V_{DS} and I_{DS}-V_{GS} curves present

appreciable values (see Fig. S10 within the Supplemental Material [25]). Additionally, Fig. S11 within the Supplemental Material [25] shows the performance comparison with other exotic 2D anti-ambipolar devices [21,22]. These main parameters and the rare bi-anti-ambipolar characteristic indicate the great potential of the 2D $InPS_3$ double subgap TFET for MVL nanoelectronics. To reveal the switching mechanism, we calculate the LDOS corresponding to five states in the OFF-ON-OFF-ON-OFF process, as depicted in Fig. S12 within the Supplemental Material [25], which is consistent with the former analysis in the schematic energy-band diagram. Nevertheless, abrupt changes in the slope are observed on either side. The challenge in reducing the I_{DS} when the V_{GS} approaches -2 and 3 V stems from the sudden alignment of the DOS peak within the channel with that in the source or drain, which increases the I_{DS}. This occurs before the DOS contributed by the HVB and LCB in the channel are fully extruded out of the tunneling window, as depicted in Fig. S13 within the Supplemental Material [25]. Moreover, from a more intuitive perspective, we also calculate the device density of states (DDOS) at V_{GS} of -4, -0.5, 0.6, 2.0, and 4.5 V, corresponding to OFF, ON, OFF, ON, OFF states, respectively, as shown in Fig. 5(d). Clearly, in the channel region, the overlap between the blue DDOS (yellow DDOS) and the green region indicates the available electron (hole) tunneling path. So, with the voltage changing from -4 to 4.5 V, OFF and ON states switch continuously due to presence of three gap states (E_{SGC}, E_g, and E_{SGV}).

IV. CONCLUSIONS

In summary, we propose a symmetry-breaking strategy in edge-sharing octahedra to design the novel metal phosphorus trichalcogenide 2D XPS_3 ($X = Al$, Ga, In, Tl) materials, which can produce isolated bands with subgap states near the Fermi level. We reveal that the split of X-s orbitals leads to the generation of isolated bands, and the different orbital interactions distinguish the characteristics of single subgap states ($AlPS_3$ and $TlPS_3$) from double subgap states ($GaPS_3$ and $InPS_3$). Moreover, based on the isolated bands, we demonstrate the device concept of double subgap TFETs to achieve the rare bi-anti-ambipolar transport behavior. The transport mechanism relies on the three gap states to block the tunneling and two isolated bands to conduct the tunneling path. Among the four 2D XPS_3 materials, $InPS_3$ possesses a symmetrical and narrow band dispersion for both ICB and IVB, thus making it an ideal example. Based on DFT NEGF computations, not only can the N-shaped and M-shaped NDR effects be achieved in the output and transfer characteristics of the 2D $InPS_3$ TFET, but the PVR, driving range, and operation voltages also demonstrate good performance. Hence, our work opens up an alternative avenue for achieving bi-anti-ambipolar transport by using the intrinsic electronic properties of 2D materials. We hope our results can inspire further experimental and theoretical exploration of the double subgap materials for developing MVL nanoelectronics.

ACKNOWLEDGMENTS

This work was financially supported by the Training Program of the Major Research Plan of the National Natural Science Foundation of China (Grants No. 91964103, No. 92164102), and the National Natural Science Foundation of China (Project No. 52202247), Doctor Start-up Fund Research supported by Jinling Institute of Technology (Project No. JIT-B-202120), the Scientific Research Fund Incubation Project of Jinling Institute of Technology (Project No. jit-fhxm-202115).

[1] S. Salahuddin, K. Ni, and S. Datta, The era of hyper-scaling in electronics, Nat. Electron. **1**, 442 (2018).
[2] A. Sebastian, M. Le Gallo, R. Khaddam-Aljameh, and E. Eleftheriou, Memory devices and applications for in-memory computing, Nat. Nanotechnol. **15**, 529 (2020).
[3] J. Shim, S. Oh, D. H. Kang, S. H. Jo, M. H. Ali, W. Y. Choi, K. Heo, J. Jeon, S. Lee, M. Kim, Y. J. Song, and J. H. Park, Phosphorene/rhenium disulfide heterojunction-based negative differential resistance device for multi-valued logic, Nat. Commun. **7**, 13413 (2016).
[4] T. Roy, M. Tosun, X. Cao, H. Fang, D. H. Lien, P. D. Zhao, Y. Z. Chen, Y. L. Chueh, J. Guo, and A. Javey, Dual-gated MoS_2/WSe_2 van der Waals tunnel diodes and transistors, ACS Nano **9**, 2071 (2015).
[5] W. Y. Fung, L. Chen, and W. Lu, Esaki tunnel diodes based on vertical Si-Ge nanowire heterojunctions, Appl. Phys. Lett. **99**, 092108 (2011).
[6] K. Kobashi, R. Hayakawa, T. Chikyow, and Y. Wakayama, Multi-valued logic circuits based on organic anti-ambipolar transistors, Nano Lett. **18**, 4355 (2018).
[7] J. Liu, J. Liu, J. Zhang, C. Li, Q. Cui, F. Teng, H. Li, and L. Jiang, High-performance n- and p-type organic single-crystal field-effect transistors with an air-gap dielectric towards anti-ambipolar transport, J. Mater. Chem. C **8**, 4303 (2020).
[8] R. Cheng, L. Yin, F. Wang, Z. Wang, J. Wang, Y. Wen, W. Huang, M. G. Sendeku, L. Feng, Y. Liu, and J. He, Anti-ambipolar transport with large electrical modulation in 2D heterostructured devices, Adv. Mater. **31**, e1901144 (2019).
[9] Y. Sun, W. Gao, X. Li, C. Xia, H. Chen, L. Zhang, D. Luo, W. Fan, N. Huo, and J. Li, Anti-ambipolar behavior and photovoltaic effect in p-$MoTe_2$/n-InSe heterojunctions, J. Mater. Chem. C **9**, 10372 (2021).
[10] Y. Li, Y. Wang, L. Huang, X. Wang, X. Li, H. X. Deng, Z. Wei, and J. Li, Anti-ambipolar field-effect transistors based on few-layer 2D transition metal dichalcogenides, ACS Appl. Mater. Interfaces **8**, 15574 (2016).
[11] Hurst, Multiple-valued logic-its status and its future, IEEE Trans. Comput. **12**, 1160 (1984).

[12] Y. Wakayama and R. Hayakawa, Antiambipolar transistor: A newcomer for future flexible electronics, Adv. Funct. Mater. **30**, 1903724 (2019).

[13] D. Wu, W. Li, A. Rai, X. Wu, H. C. P. Movva, M. N. Yogeesh, Z. Chu, S. K. Banerjee, D. Akinwande, and K. Lai, Visualization of local conductance in MoS_2/WSe_2 heterostructure transistors, Nano Lett. **19**, 1976 (2019).

[14] V. K. Sangwan, M. E. Beck, A. Henning, J. Luo, H. Bergeron, J. Kang, I. Balla, H. Inbar, L. J. Lauhon, and M. C. Hersam, Self-aligned van der Waals heterojunction diodes and transistors, Nano Lett. **18**, 1421 (2018).

[15] M. Huang, S. Li, Z. Zhang, X. Xiong, X. Li, and Y. Wu, Multifunctional high-performance van der Waals heterostructures, Nat. Nanotechnol. **12**, 1148 (2017).

[16] A. K. Paul, M. Kuiri, D. Saha, B. Chakraborty, S. Mahapatra, A. K. Sood, and A. Das, Photo-tunable transfer characteristics in $MoTe_2$-MoS_2 vertical heterostructure, npj 2D Mater. Appl. **1**, 17 (2017).

[17] S. Park, H. J. Lee, W. Choi, H. J. Jin, H. Cho, Y. Jeong, S. Lee, K. Kim, and S. Im, Quaternary NAND logic and complementary ternary inverter with p-$MoTe_2$/n-MoS_2 heterostack channel transistors, Adv. Funct. Mater. **32**, 2108737 (2021).

[18] J. H. Lim, J. Shim, B. S. Kang, G. Shin, H. Kim, M. Andreev, K. S. Jung, K. H. Kim, J. W. Choi, Y. Lee, and J. H. Park, Double negative differential transconductance characteristic: From device to circuit application toward quaternary inverter, Adv. Funct. Mater. **29**, 1905540 (2019).

[19] C. R. Paul Inbaraj, R. J. Mathew, R. K. Ulaganathan, R. Sankar, M. Kataria, H. Y. Lin, Y. T. Chen, M. Hofmann, C. H. Lee, and Y. F. Chen, A bi-anti-ambipolar field effect transistor, ACS Nano **15**, 8686 (2021).

[20] D. Panigrahi, R. Hayakawa, and Y. Wakayama, Anti-ambipolar transistor with double negative differential transconductances for organic quaternary logic circuits, Adv. Funct. Mater. **33**, 2213899 (2023).

[21] M. Andreev, J. W. Choi, J. Koo, H. Kim, S. Jung, K. H. Kim, and J. H. Park, Negative differential transconductance device with a stepped gate dielectric for multi-valued logic circuits, Nanoscale Horiz. **5**, 1378 (2020).

[22] Y. Meng, W. Wang, W. Wang, B. Li, Y. Zhang, and J. Ho, Anti-ambipolar heterojunctions: Materials, devices, and circuits, Adv. Mater. **36**, 2306290 (2023).

[23] S. Smidstrup, *et al.*, QuantumATK: An integrated platform of electronic and atomic-scale modelling tools, J. Phys.: Condens. Matter **32**, 015901 (2020).

[24] J. P. Perdew, K. Burke, and M. Ernzerhof, Generalized gradient approximation made simple, Phys. Rev. Lett. **77**, 3865 (1996).

[25] See Supplemental Material http://link.aps.org/supplemental/10.1103/PhysRevApplied.21.064009 for electronic structures of $InPS_3$ in different basis sets; variation of material structural parameters; projected band structures of X-s orbitals in different lattices; band structures with and without spin-orbit coupling; energy-level-aligned PDOS and partial charge densities; band alignment of XPS_3; phonon dispersion of $InPS_3$; schematic of the device; relationship between V_{DS} and V_{GS}; subthreshold swing of I-V curves; comparison of device performance; LDOS corresponding to the OFF-ON-OFF-ON-OFF process; reason for sudden change of slope; electronic parameters of XPS_3.

[26] M. Buttiker, Y. Imry, R. Landauer, and S. Pinhas, Generalized many-channel conductance formula with application to small rings, Phys. Rev. B **31**, 6207 (1985).

[27] F. Wang, T. A. Shifa, P. Yu, P. He, Y. Liu, F. Wang, Z. Wang, X. Zhan, X. Lou, F. Xia, and J. He, New frontiers on van der Waals layered metal phosphorous trichalcogenides, Adv. Funct. Mater. **28**, 1802151 (2018).

[28] G. Ouvrard, R. Brec, and J. Rouxel, Structural determination of some MPS_3 layered phases (M = Mn, Fe, Co, Ni and Cd), Mater. Res. Bull. **20**, 1181 (1985).

[29] B. L. Chittari, Y. Park, D. Lee, M. Han, A. H. MacDonald, E. Hwang, and J. Jung, Electronic and magnetic properties of single-layer MPX_3 metal phosphorous trichalcogenides, Phys. Rev. B **94**, 184428 (2016).

[30] S. Lee, The MPS_3 Coloring Problem, J. Am. Chem. Soc. **110**, 8000 (1988).

[31] E. Prouzet, G. Ouvrard, and R. Brec, Structure determination of $ZnPS_3$, Mater. Res. Bull. **21**, 195 (1986).

[32] G. Tang, P. Ghosez, and J. Hong, Band-edge orbital engineering of perovskite semiconductors for optoelectronic applications, J. Phys. Chem. Lett. **12**, 4227 (2021).

[33] C. Huang, J. Feng, J. Zhou, H. Xiang, K. Deng, and E. Kan, Ultra-high-temperature ferromagnetism in intrinsic tetrahedral semiconductors, J. Am. Chem. Soc. **141**, 12413 (2019).

[34] L. D. Yuan, H. X. Deng, S. S. Li, S. H. Wei, and J. W. Luo, Unified theory of direct or indirect band-gap nature of conventional semiconductors, Phys. Rev. B **98**, 245203 (2018).

[35] M. H. Whangbo, R. Brec, G. Ouvrard, and J. Rouxel, Reduction sites of transition-metal phosphorus trichalcogenides, MPX_3, Inorg. Chem. **24**, 2459 (1985).

[36] A. M. Ionescu and H. Riel, Tunnel field-effect transistors as energy-efficient electronic switches, Nature **479**, 329 (2011).

[37] W. Cao, J. Jiang, J. Kang, D. Sarkar, W. Liu, and K. Banerjee, in *2015 IEEE International Electron Devices Meeting (IEDM)* (IEEE, Washington, DC, 2015), pp. 12.3.1.